

Received 12 November 2023, accepted 29 November 2023, date of publication 30 November 2023, date of current version 8 December 2023.

Digital Object Identifier 10.1109/ACCESS.2023.3338355

## RESEARCH ARTICLE

# Edge Detection of High-Resolution Remote Sensing Image Based on Multi-Directional Improved Sobel Operator

LU SHI<sup>1</sup>, (Student Member, IEEE), AND YUEFENG ZHAO, (Member, IEEE)

Shandong Provincial Engineering and Technical Center of Light Manipulations & Shandong Provincial Key, Jinan 250014, China  
Laboratory of Optics and Photonic Device, School of Physics and Electronics, Shandong Normal University, Jinan 250014, China

Corresponding author: Yuefeng Zhao (yuefengzhao@sdu.edu.cn)

This work was supported in part by the National Natural Science Foundation of China under Grant 62002208 and Grant 42271093, and in part by the Natural Science Foundation of Shandong Province under Grant ZR2019MA028 and Grant ZR2020MA082.

**ABSTRACT** Automatic detection of building edge information from high-resolution remote sensing images can more accurately obtain building distribution information, which is of great significance for urban land planning, urban building planning and population estimation. The satellite image will be affected by atmospheric interference and noise, we preprocess the image to eliminate the atmospheric interference such as atmospheric correction and radiometric calibration, and utilize a new total variation and wavelet adaptive thresholding hybrid filter proposed in this paper to achieve the filtering of noise while retaining the image edge detail information. The traditional detection operator is prone to the problems of scattered edge points, discontinuity or misjudgment of too many edge points in the detection results due to the limitations of directions, template sizes. Therefore, this paper proposes a new 16-direction  $5 \times 5$  size Sobel operator to replace the previous Sobel operator with only horizontal and vertical directions, using these 16 directions to calculate the gradient of each pixel points. And each direction template is extracted to each direction contour image for weighted fusion. Thus, the edge information of different angles can be extracted, and the all-round information edge extraction of the image can be realized. By comparing the experimental visual effect and the evaluation criteria of the data results, the SNR, PSNR, AUC, and FOM values of the improved algorithm are much higher than other algorithms, with the advantage of higher image detection edge positioning accuracy, more complete contour lines and stronger anti-interference ability.

**INDEX TERMS** Edge detection, multi-directional, remote sensing images, Sobel operator, total variance, wavelet adaptive threshold.

## I. INTRODUCTION

With the continuous development of digital information technology, edge detection technology takes the image to be detected as a carrier for information transfer, extracts the useful signal of the image to be detected, and is used to realize the precise positioning of the edge of the target image [1]. Edge detection is the main feature extraction tool used for image analysis and pattern recognition [2]. Good edge detection can quickly and accurately identify image edge information, providing rich intrinsic information about image orientation, step

attributes and shape. Edge detection technology is utilized to mine the rich feature information in satellite images for urban planning [3], city mapping [4], change detection and other fields [5], [6], [7].

In recent decades, the detection of buildings, roads and other common features in China and many other countries has been mainly based on manual field mapping, which has the disadvantages of high cost and time-consuming. With the continuous development of remote sensing and space technology, remote sensing can provide detailed information on common features [8], while the capability of satellites to acquire ground feature information has been improved. At present, the spatial resolution of many satellites has

The associate editor coordinating the review of this manuscript and approving it for publication was Sudhakar Radhakrishnan<sup>1</sup>.

reached the sub-meter level, and satellite images have rich spatial and geometric features [9], making it possible to use remote sensing satellite images to detect feature edge information. At the same time, relying on computer technology, it is possible to realize the extraction of inland feature information in the required area in a very short time. In order to reduce labor cost and time loss, accurately identifying feature edges of features from high-resolution remote sensing (HRS) images and extracting building edges from them is an important challenge and also a research hotspot in the field of remote sensing [10].

In recent years, researchers have been proposing different algorithms to realize the extraction of feature information edges from high-resolution remote sensing images, but there are still problems such as low accuracy and incomplete edge detection [11], [12], [13], [14]. Traditional edge detection algorithms include Prewitt [15], Roberts [16], Sobel [17], Canny [18], Log [19] operators and so on. These operators usually use spatial convolution methods that utilize a template convolution kernel to be convolved with the image to extract edges. These operators have a wide range of applicability and fast computation speed, but less consideration is given to the image edge direction features, and it is easy to lose the edge detail information [15]. Tavakoli et al. [20] devised a hierarchical scheme that iteratively adjusts the probability of being assigned to different features, resulting in a kind of decision tree that recognizes edges of buildings and roads in satellite imagery, but it is generally ineffective and fails to recognize small-area edge features. Zhang et al. [11] added two direction information of  $45^\circ$  and  $135^\circ$  on the basis of the Sobel algorithm, so that the detection accuracy has been improved, but the improvement effect is general. Han et al. [21] expanded the original Sobel algorithm direction template to eight directions, the ability of edge detection is improved, but it is sensitive to noise and prone to identify pseudo edges. Chetia et al. [22] iteratively form a new image by firstly iterating the gray value and pixel coordinates of the image, and then expand the Sobel algorithm, which has only horizontal and vertical orientations, to four horizontal, vertical,  $45^\circ$ , and  $135^\circ$  orientations to obtain the final edge detection result by using the non-maximum value suppression. This algorithm improves the circuit complexity, but does not take into account the noise affecting the edge information, and the noise immunity is poor. Liu et al. [23] expand the eight-direction Sobel operator on the basis of Chetia and utilize the double-threshold detection method. Kong et al. [24] apply the improved genetic algorithm to different images to obtain different thresholds for the Sobel edge detection, and the resulting edge continuity is good, but the noise immunity is poor, and the detection accuracy is not high. Robertas et al. [25] used good random projection and kernel density estimation to identify the outliers in the two-dimensional projection of image point features as significant image points, and the method can identify part of the information content. Xie et al. [26] proposed an edge

detection algorithm to solve the blurring of edges and object boundaries using a deep learning model with full convolution neural networks and deep supervised networks. Li et al. [27] combined the traditional operator and deep learning methods, but this method needs to manually sort the samples according to the relative value of the image classification probability, which is manually labor-intensive and can not identify the specific detail information.

Another part of the researchers will improve the algorithm based on improving the noise immunity of the image to improve the detection accuracy of the algorithm. Topno et al [12] performed median filtering on the image before the edge detection, filtered out the pretzel noise in the image, and then detected the edge of the image by using the Canny algorithm, which has a general effect. Sung et al. [13] processed the image first using a bilateral filter that reduces the blurring of image edges, then utilized the Canny operator, and finally processed the results using morphological properties. The edge region obtained by this algorithm is continuously faulted. Shekhar et al. [28] processed the image using Gaussian filter and then chose different scales of Sigma values and thresholds for edge detection. The algorithm considered too few directions of information and the detection accuracy was average. Tian et al. [29] proposed a weighted kernel paradigm minimization denoising algorithm to improve the noise immunity of the Sobel algorithm so as to optimize the edge detection effect. Although the algorithm has strong noise immunity, it does not take into account the multi-directional edge information of the image, and there is still room for improvement in the edge detection effect of the image.

The main purpose of this paper is to propose an edge detection algorithm for HRS images, especially for the problems such as incomplete recognition of edge information and easy omission of small region information. The presence of noise in HRS images affects the integrity of edge detection, so in this paper, a hybrid filter with total variation (TV) and wavelet adaptive threshold denoising (WATD) is proposed for filtering noise in HRS images to improve the noise immunity of the algorithm. This paper also expands the direction template to 16 directions on the basis of the Sobel algorithm, proposes a new type of  $5 \times 5$  gradient template according to the different weight distributions, and then refines the edges by using non-maximum value suppression and 2D otsu thresholding to obtain the final detection results. The experiment proves that the algorithm has a good ability to suppress noise, can obtain clear edges in noisy images, and has a good edge detection ability, thus verifying the effectiveness and accuracy of the algorithm.

In Section II, we describe in detail the hybrid total variation and wavelet adaptive threshold denoising methods. We introduce the novel 16-direction Sobel algorithm in Section III. The results and analysis of different denoising methods and different edge detection algorithms for different images are obtained in Section IV and concluded in Section V.

## II. THE HYBRID DENOISING WITH WAVELET ADAPTIVE THRESHOLDING AND TOTAL VARIATIONAL

The realization of HRS image denoising needs to maintain image edges and important feature information in order to achieve more accurate edge information detection. Wavelet thresholding denoising is prone to cause edge blurring, and the total variation denoising suffers from insufficient denoising of smooth regions of the image. Therefore, we propose a hybrid denoising method with total variation and improved wavelet adaptive threshold denoising.

### A. THE WAVELET ADAPTIVE THRESHOLDING DENOISING

The principle of wavelet thresholding noise reduction [30] is to estimate the threshold value after wavelet decomposition of the image containing noise, where the larger coefficients are mainly real and useful information, while those smaller coefficients are most likely to be noise information. The wavelet coefficients associated with noise are processed using the shrinkage principle, which means that the coefficients are appropriately weighted or set to zero, and then the recalculated wavelet coefficients are combined with the image to perform wavelet reconstruction, so that the denoised image can be obtained [31].

It is assumed that the noisy image  $Y = (y_n)_{n \in [1, n]}$  is an observation of the original image  $X = (x_n)_{n \in [1, n]}$ , and then  $Y = X + \sigma^2 Z$ . Where,  $\sigma^2$  is the noise variance and  $Z = (Z_n)_{n \in [1, n]}$  is an independent identically distributed Gaussian white noise. The noisy image after wavelet transform can be represented in the wavelet domain as  $W_i = F_i + \sigma^2 Z_i$ ,  $i \in [1, n]$ .  $W_i, F_i$  are the wavelet coefficients of the noise-containing image and the original image, respectively, and the white noise  $Z_i$  remains white noise in the wavelet domain after the white noise transform  $Z_i$ . The correlation process is then performed on  $W_i$ , and the denoised image  $W_i$  is obtained by the reconstruction  $X'$  after the process.

The common shrinkage principles are soft threshold function and hard threshold function methods, where the soft threshold function [32] is

$$\tilde{W}_{Soft} = \begin{cases} \text{sgn}(W) (|W| - T), & |W| > T \\ 0 & , |W| \leq T, \end{cases} \quad (1)$$

and the hard threshold function [33] is

$$\tilde{W}_{Hard} = \begin{cases} W, & |W| > T \\ 0, & |W| \leq T. \end{cases} \quad (2)$$

where,  $W$  is the wavelet transform coefficients of the noisy image,  $\tilde{W}$  is the wavelet coefficients processed by the threshold function and  $T$  is the threshold value.

The image processed by the soft threshold function causes some degree of blurring of edges and other phenomena. The hard threshold function does not change the wavelet coefficients in this part, but it is not continuous at the threshold point, and the image processed by this threshold function will have oscillations and pseudo-Gibbs effect [33].

Therefore, a wavelet adaptive threshold denoising function is proposed, which is expressed as follows:

$$\tilde{W}_{Adaptive} = \begin{cases} \text{sgn}(W) \lambda (|W| - \phi T) \\ 0. \end{cases} \quad (3)$$

where,  $\lambda = \begin{cases} 1, & |W| \geq T \\ \frac{T}{T-T_0}, & T_0 \leq |W| < T, T_0 = \theta T, \theta \text{ is a} \\ 0, & |W| < T_0 \end{cases}$  random parameter,  $W$  is the wavelet transform coefficients of the noisy image,  $\tilde{W}$  is the wavelet coefficients processed by the threshold function and  $T$  is the threshold value.

The wavelet adaptive thresholding method is used to shrink to 0, and the threshold function is adjusted by introducing the weight function, which can keep the image edge details and filter out the noise at the same time, so that the image is smoother and has better continuity. At the same time, we use the GGD model to estimate the threshold value, the coefficients of the subbands other than LL of the image wavelet decomposition are basically symmetrically distributed near 0, and a spike is formed at the zero point. Therefore, it can be described by the zero-mean generalized Gaussian distribution GGD [34]:

$$GG_{\beta, \sigma_x}(x) = C(\beta, \sigma_x) e^{-(\partial(\beta, \sigma_x)|x|)^\beta}, \quad (4)$$

where,  $-\infty < x < +\infty, \sigma_x > 0, \beta > 0$ ,  $\partial(\beta, \sigma_x) = \sigma_x^{-1} \left[ \frac{\Gamma(3/\beta)}{\Gamma(1/\beta)} \right]^{\frac{1}{2}}$ ,  $C(\beta, \sigma_x) = \frac{\beta \partial(\beta, \sigma_x)}{2\Gamma(1/\beta)}$ .  $\Gamma(t) = \int_0^\infty e^{-u} u^{(t-1)} du$  is the  $\Gamma$  function,  $\beta$  is the shape parameter of GGD, and  $\sigma_x$  is the standardized variance. Obviously,  $\beta = 1$  is Laplace distribution and  $\beta = 2$  is Gaussian distribution.

A threshold expression for the GGD model was given by Chang et al. [35]:

$$T = \sigma^2 \sqrt{\partial}, \quad (5)$$

where  $\partial$  is the standard deviation of the signal,  $\sqrt{\partial} = 1/\sigma_x$ , and hence  $T = \frac{r\sigma_n^2}{\sigma_x} \cdot \sigma_n^2$  is the noise variance, and  $r$  is the adjustable parameter.

By utilizing the robust median estimate  $\sigma_n^2$  proposed by Donoho [30]:

$$\sigma_n^2 = \text{Median}(|W_x(i, j)|) / 0.6745, W_x(i, j) \in HH_1, \quad (6)$$

For the standard deviation  $\sigma_x$ , the value of  $\sigma_x$  varies with the scale, and the variance of the images at different spatial locations within the same wavelet decomposition subband varies with a large difference. Therefore, it is not reasonable to use the same  $\sigma_x$  estimation within the same subband, which can easily lead to the loss of image detail information. For this reason, this paper adopts a variance estimation method characterized by spatial local adaptation. It is assumed that the variance of the domain coefficients of the wavelet coefficients is strongly correlated, and the variance estimation is performed based on the local domain information of the

wavelet subband coefficients in terms of subbands. The current wavelet subband coefficients are assumed as  $W_x(i, j)$ , and the variance of their local domain is defined as follows:

$$\sigma_y^2(i, j) = \frac{1}{M} \sum_{(k,r) \in N(i,j)} W_x^2(k, r), \quad (7)$$

where,  $N(i, j)$  is the local domain window centered on  $W_x(i, j)$  and  $M$  is the number of wavelet subband coefficients in window  $N(i, j)$ . The signal variance of the coefficients is:

$$\sigma_x(i, j) = \sqrt{\max(\sigma_y^2(i, j) - \sigma_n^2, 0)}, \quad (8)$$

The final adaptive optimal threshold  $T$  is obtained as:

$$T = \frac{r\sigma_n^2}{\sigma_x(i, j)}. \quad (9)$$

### B. THE TOTAL VARIATION MODEL DENOISING

The anisotropic diffusion equation of partial differential equation is introduced into the total variation model [36] for image denoising. While smoothing the noise, the edge can be preserved and some details of the image can be preserved.

We assume that image  $X(i, j)$  is the original image,  $Z(i, j)$  is the Gaussian noise, and  $Y_n(i, j)$  is the image containing the noise as shown in the following equation:

$$Y_n(i, j) = X(i, j) + Z(i, j), \quad (10)$$

The total variant of the image  $X(i, j)$  is defined as [37]:

$$TV(X) = \int_{\omega} |\nabla X| dx dy + \frac{\sigma}{2} \int_{\omega} (X - X_n)^2 dx dy. \quad (11)$$

where,  $X$  is the image without noise,  $X_n$  is the observed noisy image,  $\int_{\omega} |\nabla X| dx dy$  is the regular term, which mainly serves to suppress the noise.  $\int_{\omega} (X - X_n)^2 dx dy$  is the fidelity term, which mainly serves to retain the original characteristics of the image in order to remove the noise as close as possible to the original image  $\sigma > 0$  is the parameter that balances the regular term and the fidelity term.

The Eq.(11) is transformed into the solution of the equation  $\frac{\partial X}{\partial t} = -div\left(\frac{\nabla X}{|\nabla X_n|}\right) + \sigma(X - X_n)$ , so as to solve the corresponding functional Euler-Lagrange equation:

$$-\nabla\left(\frac{\nabla X}{|\nabla X_n|}\right) + \sigma(X - X_n) = 0. \quad (12)$$

According to Eq. (12), the diffusion coefficient is  $\frac{1}{|\nabla X|}$ . In this paper, the number of iterations is set to 15 and  $\frac{1}{|\nabla X|}$  to 0.03. In the edge region of the image, the gradient modulus is larger and the diffusion coefficient is smaller, thus better protecting the edge information of the image. In the flat region of the image, the gradient modulus value is smaller and the diffusion coefficient is larger to smooth out the noise in the image as much as possible.

### C. HYBRID DENOISING WITH WAVELET ADAPTIVE THRESHOLDING AND TOTAL VARIATION MODELING

The wavelet threshold denoising method can remove Gaussian noise and has a very good effect in the flat area of the image. However, selecting an inappropriate threshold will excessively affect the wavelet coefficients, resulting in image edge blur and image distortion. The total variation method will not affect the image edge information, but the noise processing effect in the flat area of the image is not good, and the pseudo-edge phenomenon is easy to occur. Therefore, we propose a hybrid denoising method of wavelet adaptive threshold denoising and total variation model based on the characteristics that wavelet threshold has good denoising effect in flat area and total variation model can protect image edge information. It can not only completely filter out noise, but also the image edge information can be preserved with better continuity.

The steps and method flow chart of wavelet adaptive threshold denoising and total variation model hybrid denoising are as follows:

(1) Using wavelet adaptive threshold denoising and total variation denoising model to denoise the HRS image containing noise, the denoised image  $W$  and  $T$  are obtained respectively.

(2) A layer of wavelet decomposition is performed on the image  $W$  denoised by wavelet adaptive threshold denoising method and the image  $T$  denoised by total variation model using Haar's small fundamental wavelet in wavelet decomposition, respectively. And then a low-low frequency decomposition sub-image CA1 and CA2, a low-high frequency decomposition sub-image CH1 and CH2, a high-low frequency decomposition sub-image CV1, CV2 and a high-frequency sub-image CD1, CD2 are obtained, respectively.

(3) Choosing the low-frequency sub-image CA1 with good denoising effect and the high-frequency sub-images CH2, CV2, CD2 with complete edge information to form new 4 sub-images.

(4) Reconstruct the new 4 sub-images using wavelet inverse transform to get the final image with complete edge information and better denoising effect.

## III. THE NOVEL 16-DIRECTION SOBEL OPERATOR EDGE DETECTION

### A. TRADITIONAL SOBEL OPERATOR

Assuming that the original image  $X$  function is  $P(x, y)$ , the gradient  $P'(x, y)$  of the image at  $(x, y)$  is a vector representing the direction and magnitude as shown in (13).

$$P'(x, y) = \frac{\partial P}{\partial x}m + \frac{\partial P}{\partial y}n, \quad (13)$$

where,  $m$  and  $n$  denote the horizontal vectors in the  $x$  and  $y$  directions, respectively.

The edge data of image  $X$  at  $(x, y)$  is represented by the amplitude  $Grad$  of the gradient operator. The amplitude  $Grad$



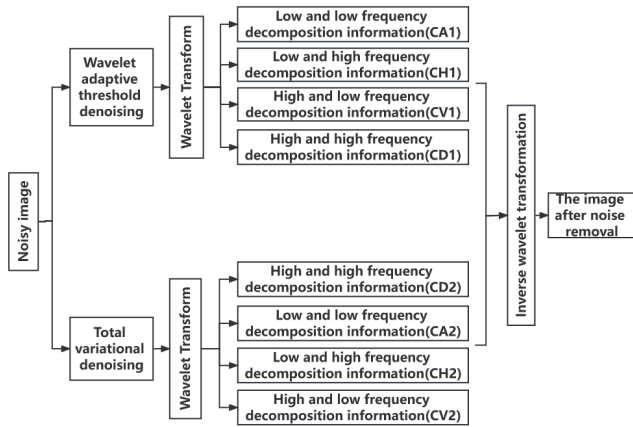


FIGURE 1. The flowchart of the hybrid denoising method of WATD and TV modeling.

and the direction are shown as follows [17]:

$$Grad = \left[ \left( \frac{\partial P}{\partial x} \right)^2 + \left( \frac{\partial P}{\partial y} \right)^2 \right]^{\frac{1}{2}}, \quad (14)$$

$$\theta = \arctan \left[ \left( \frac{\partial P}{\partial y} \right) \div \left( \frac{\partial P}{\partial x} \right) \right]. \quad (15)$$

We assume that the original image

$$X = \begin{bmatrix} f(x-1, y-1) & f(x, y-1) & f(x+1, y-1) \\ f(x-1, y) & f(x, y) & f(x+1, y) \\ f(x-1, y+1) & f(x, y+1) & f(x+1, y+1) \end{bmatrix}.$$

The vertical and horizontal gradients of the Sobel operator are  $G_x$  and  $G_y$  [23], which denote the gray values of the edge detection image in the vertical and horizontal directions, respectively.

$$\begin{aligned} G_x &= Sobel_x \times A \\ &= f(x+1, y-1) + 2f(x+1, y) + f(x+1, y+1) \\ &\quad - f(x-1, y-1) - 2f(x-1, y) - f(x-1, y+1) \\ &= \begin{bmatrix} 1 & 0 & -1 \\ 2 & 0 & -2 \\ 1 & 0 & -1 \end{bmatrix}, \end{aligned} \quad (16)$$

$$\begin{aligned} G_y &= Sobel_y \times A \\ &= f(x-1, y+1) + 2f(x, y+1) + f(x+1, y+1) \\ &\quad - f(x-1, y-1) - 2f(x-1, y) - f(x+1, y-1) \\ &= \begin{bmatrix} 1 & 2 & 1 \\ 0 & 0 & 0 \\ -1 & -2 & -1 \end{bmatrix}. \end{aligned} \quad (17)$$

Thus, the horizontal and vertical convolution kernel templates for the Sobel operator are shown below.

The traditional Sobel operator calculates the extreme value at the edge according to the weighted difference between the upper and lower, left and right adjacent points, so as to detect the edge and obtain a more continuous edge. Since the Sobel operator only considers the gradients in the horizontal and vertical directions, the edge gradient information is too little, resulting in incomplete edge detection.

### B. EDGE DETECTION ALGORITHM BASED ON 16-DIRECTION SOBEL OPERATOR

The traditional Sobel operator utilizes a convolutional kernel of  $3 \times 3$  size in the X and Y directions as a gradient template, which can only detect the edges in the horizontal and vertical directions, with low edge localization accuracy, and some detail information is lost, making the edges somewhat blurred. By extending Sobel to four direction detection templates of  $0^\circ$ ,  $45^\circ$ ,  $90^\circ$  and  $135^\circ$  [5] (as shown in Fig. 3), the obtained edge information is significantly improved, but there are still some problems of missed detection and poor noise immunity. The common convolution kernel sizes used for edge detection are  $3 \times 3$ ,  $5 \times 5$  and  $7 \times 7$ . The size of  $5 \times 5$  convolution kernel is more effective than  $3 \times 3$  convolution kernel in feature extraction. Under the same noise intensity, the  $5 \times 5$  convolutional kernel is more noise-resistant and more suitable for remote sensing images containing more complex feature information, realizing a smoother image effect and helping to subsequently extract clearer edge features. The features extracted by  $5 \times 5$  convolution kernel will be more accurate than  $7 \times 7$  size,  $7 \times 7$  convolution kernel will ignore some detailed information in the image, so it is not the larger the convolution kernel the better.  $7 \times 7$  size convolution kernel will take longer to process the image, it is not applicable to remote sensing images. Therefore, we propose a new 16-direction  $5 \times 5$  size convolution kernel as a gradient operator, the larger value of the center point of the  $5 \times 5$  size gradient operator can enhance the response of the edge, and the change of the surrounding value controls the sensitivity of the edge detection can capture the change of more pixel values, and detect more subtle edges, providing more accurate edge detection results. The  $5 \times 5$  size of the gradient operator can capture more information in the image, and extend the operator templates to  $0^\circ$ ,  $22.5^\circ$ ,  $45^\circ$ ,  $67.5^\circ$ ,  $90^\circ$ ,  $112.5^\circ$ ,  $135^\circ$ ,  $157.5^\circ$ ,  $180^\circ$ ,  $202.5^\circ$ ,  $225^\circ$ ,  $247.5^\circ$ ,  $270^\circ$ ,  $292.5^\circ$ ,  $315^\circ$  and  $337.5^\circ$  for these 16 directions, iterating multiple directions can obtain edge information in multiple directions. This algorithm is verified by simulated images to detect more complete edge information, continuous and clear contour lines, and better noise immunity.

The common Sobel operator in Fig.2 is usually used for natural images. The size of the convolution kernel is too close, which is not suitable for HRS images containing complex ground object information, and the edge information extraction of HRS images is incomplete. Therefore, according to the different city distances from the template to the center template at different positions, the weights under different coordinates are related to the city distance. We propose a novel Sobel operator with  $5 \times 5$  convolution kernel in the  $0^\circ$  and  $90^\circ$  directions as shown in the following equation:

$$Sobel_x = [1 \ 4 \ 6 \ 4 \ 1] * \begin{bmatrix} 0 \\ -1 \\ 0 \\ 1 \\ 0 \end{bmatrix}$$

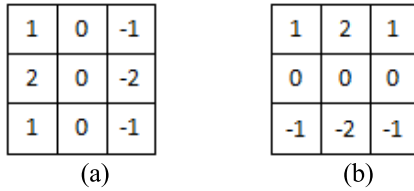


FIGURE 2. The convolution kernel templates: (a) The horizontal 0° direction template. (b) The vertical 90° direction template.

$$= \begin{bmatrix} 0 & 0 & 0 & 0 & 0 \\ -1 & -4 & -6 & -4 & -1 \\ 0 & 0 & 0 & 0 & 0 \\ 1 & 4 & 6 & 4 & 1 \\ 0 & 0 & 0 & 0 & 0 \end{bmatrix}, \quad (18)$$

$$Sobel_y = \begin{bmatrix} 1 \\ 4 \\ 6 \\ 4 \\ 1 \end{bmatrix} * [0 \ -1 \ 0 \ 1 \ 0]$$

$$= \begin{bmatrix} 0 & -1 & 0 & 1 & 0 \\ 0 & -4 & 0 & 4 & 0 \\ 0 & -6 & 0 & 6 & 0 \\ 0 & -4 & 0 & 4 & 0 \\ 0 & -1 & 0 & 1 & 0 \end{bmatrix}. \quad (19)$$

The novel 5 × 5 convolutional kernel proposed in this paper can capture more target pixel information, better detect longer edges and larger object boundaries in HRS images, and capture more detailed textures at the same time. The 5 × 5 convolutional kernel has better robustness to noise and subtle changes when processing images.

The new Sobel operator convolution kernel template for different directions is obtained by rotating  $Sobel_x$  in 16 directions as shown below:

The gray values of each pixel in 16 directions are combined to obtain the gray value of each pixel in the image:

$$G = \sqrt{G_0^2 + G_{22.5}^2 + G_{45}^2 + \dots + G_{292.5}^2 + G_{315}^2 + G_{337.5}^2}. \quad (20)$$

The main steps of the multi-directional improved Sobel operator (MISA) for the pre-processed image edge detection method are as follows:

(1) The matrix  $[M]^n$  is used to represent the detection templates in the above 16 directions, where n is the detection direction of the template, and the value of n is 1, 2, ..., 16.

$$[M]^n = \begin{bmatrix} M_{-x,-y}^n & \dots & M_{-x,y}^n \\ \vdots & M_{0,0}^n & \vdots \\ M_{x,-y}^n & \dots & M_{x,y}^n \end{bmatrix}. \quad (21)$$

(2) Assuming that  $G(i, j)$  is a pre-processed denoised HRS image, the matrix  $[G(i, j)]_m$  is a 5 × 5 size window matrix of

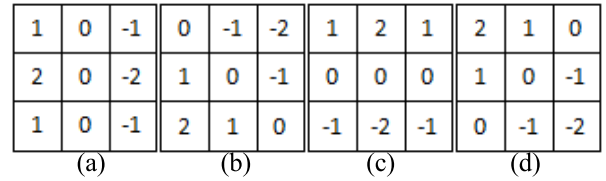


FIGURE 3. The convolutional kernel template: (a) 0° direction template. (b) 45° direction template. (c) 90° direction template. (d) 135° direction template.

the denoised HRS image, where m=5;

$$G(i, j)_m = \begin{bmatrix} g(i-x, j-y) & \dots & g(i-x, j+y) \\ \vdots & g(i, j) & \vdots \\ g(i+x, j-y) & \dots & g(i+x, j+y) \end{bmatrix}. \quad (22)$$

(3) The 16-direction gradient operator detection template  $[M]^n$  is sequentially shifted by one pixel position on the remote sensing image  $G(i, j)$  in sequence, respectively. Then convolve  $[M]^n$  and the corresponding window matrix  $[G(i, j)]_m$  with the following convolution operation:

$$G_n(i, j) = \sum_{-k}^k \sum_{-l}^l g(i+x, j+y) M_{x,y}^n. \quad (23)$$

where,  $G_n(i, j)$  is the value of the pixel at the center point of the window matrix corresponding to the detection template in the nth direction, and the value of n is 1, 2, ..., 16. The center pixel point (i,j) is at a distance k from both sides of the image in the horizontal direction and l from both sides of the image in the vertical direction.

(4) To obtain the maximum of the absolute values of the 16 gradient values by comparison, which will be used as the new pixel value of the center point (i,j) of the window matrix, as follows:

$$g(i, j) = \max [|g_n(i, j)|]. \quad (24)$$

(5) Using non-maximal suppression of output edges and choosing the 2D Otsu thresholding method to set an appropriate threshold T, making a comparison of the gray scale size with the gray scale value  $g(i, j)$  of the new pixel point. If the size of the  $g(i, j)$  value is not less than T, the pixel point is considered to be an image edge point and the pixel point is output as 1 and otherwise is output as 0.

#### IV. EXPERIMENTAL RESULTS AND ANALYSIS

In this paper, the HRS images from Gaofen-1 and WorldView-3 satellites are selected as the experimental data, mainly for the purpose of realizing the accurate detection of the edges of the HRS images, and extracting the information of the image features. In order to remove the interference of the atmosphere on image edge detection, we first selected the

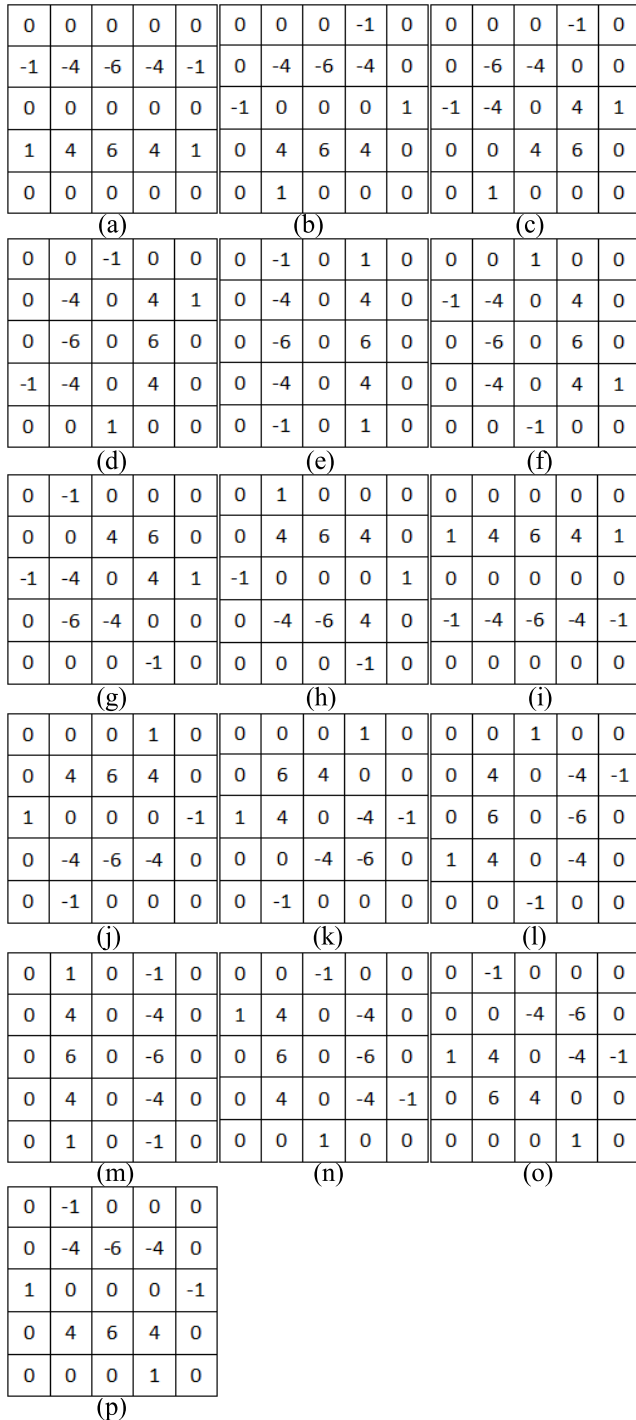


**FIGURE 4.** Sixteen directional convolutional kernel templates: (a)  $0^\circ$  inspection template. (b)  $22.5^\circ$  inspection template. (c)  $45^\circ$  inspection template. (d)  $67.5^\circ$  inspection template. (e)  $90^\circ$  inspection template. (f)  $112.5^\circ$  inspection template. (g)  $135^\circ$  inspection template. (h)  $157.5^\circ$  inspection template. (i)  $180^\circ$  inspection template. (j)  $202.5^\circ$  inspection template. (k)  $225^\circ$  inspection template. (l)  $247.5^\circ$  inspection template. (m)  $270^\circ$  inspection template. (n)  $292.5^\circ$  inspection template. (o)  $315^\circ$  inspection template. (p)  $337.5^\circ$  inspection template.

Gaofen-1 and WorldView-3 satellite images with 0% cloud shadow as the dataset in this comparison experiment, and then pre-processing operations such as atmospheric correction and

radiometric calibration were carried out on the dataset, so as to remove the influence of the atmosphere and clouds on the clarity of the images.

#### A. EFFECTIVENESS AND ANALYSIS OF DIFFERENT DENOISING METHODS

The acquisition of HRS satellite images is prone to noise, in order to verify the effectiveness of the novel total variation (TV) and wavelet adaptive thresholding (WATD) hybrid denoising method proposed in this paper, the method proposed in this paper and other four common denoising methods [32], [33], [38], [39] are applied to four HRS images for comparison experiments respectively. Test figure A is a WorldView-3 satellite image of  $395 \times 532$  pixel size with 0.4m spatial resolution. Test figure B is a Gaofen-1 satellite image with  $250 \times 252$  pixel size and 2m spatial resolution. Test figure C is a WorldView-3 satellite image of  $243 \times 257$  pixels. Test figure D is a  $194 \times 177$  pixel size Gaofen-1 satellite image. Test figure E is a  $442 \times 492$  pixel size WorldView-3 satellite image. The result maps obtained from Test figure A, B, C, D, E according to different denoising methods are shown in Fig. 5, 6, 7, 8, 9.

By analyzing the Fig. 5 - 9 visually, we found that the hard threshold denoising method will have the phenomenon of local jitter and discontinuity at the threshold, which will interfere with the detection of edge information. The soft threshold denoising method is continuous but has a large error, and the color of the processed image is too dark, which causes serious interference to the subsequent image edge detection. The compromise threshold denoising method can effectively filter out the noise, but introduces artifacts, resulting in localized distortion of the image and blurred edges. Although the global threshold denoising method can retain the image edge feature information, the denoising effect is not good in the smooth part of the image. The novel hybrid total variation and wavelet adaptive threshold method proposed in this paper can not only retain the image edge feature information, but also filter out the Gaussian noise without producing artifacts.

In order to quantitatively analyze and compare the detection results of different denoising methods in the experiments from the data, we measure the average degree of difference between the denoised image and the real image by using the mean absolute error (MAE), the mean square error (MSE) [40] and the normalized mean square error (NMSE) [41]. The smaller the MAE, MSE and NMSE, the better the denoising effect is. Meanwhile, the signal-to-noise ratio (SNR) [42] is utilized to measure the relative intensity between the useful information and noise in the image, thus reflecting the clarity of the image. The peak signal-to-noise ratio (PSNR) [40], [43] is used as an image quality evaluation metric to convert the image quality into a numerical value. The higher the PSNR, the better the image quality and the lower the distortion level. The data comparison and analysis of the result graphs of Test figures A-E under different denoising methods using the five evaluation indexes of MAE, MSE,

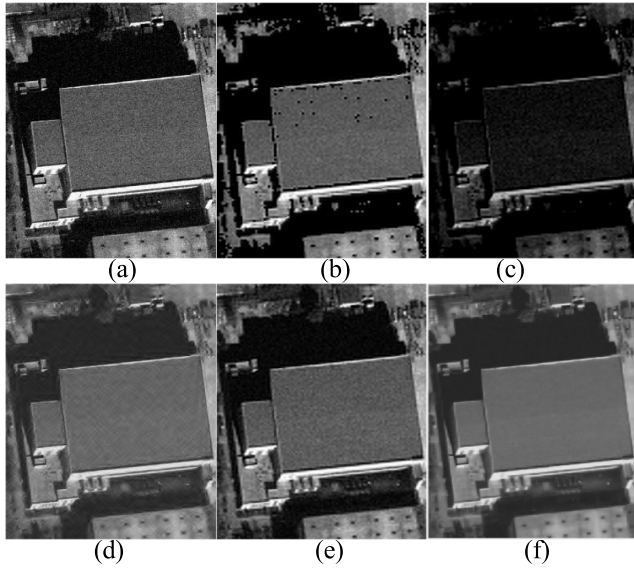


**FIGURE 5.** The results of different denoising algorithms on the Test figure A. (a) Image with Gaussian noise. (b) Hard threshold denoising result graph. (c) Soft threshold denoising result map. (d) Folding threshold denoising result graph. (e) Global threshold denoising result map. (f) Novel TV and WATD hybrid denoising result plot.

NMSE, SNR and PSNR are shown in Table 1 - 5.

$$MAE = \frac{\sum_{i=0}^{m-1} \sum_{j=0}^{n-1} |R(i, j) - P(i, j)|}{m \times n}, \quad (25)$$

$$MSE = \frac{1}{m \times n} \sum_{i=0}^{m-1} \sum_{j=0}^{n-1} [R(i, j) - P(i, j)]^2, \quad (26)$$

$$NMSE = \frac{\sum_{i=0}^{m-1} \sum_{j=0}^{n-1} [R(i, j) - P(i, j)]^2}{\sum_{i=0}^{m-1} \sum_{j=0}^{n-1} [P(i, j)]^2}, \quad (27)$$

$$SNR = 10 \log_{10} \frac{\sum_{i=0}^{m-1} \sum_{j=0}^{n-1} [P(i, j)]^2}{\sum_{i=0}^{m-1} \sum_{j=0}^{n-1} [R(i, j) - P(i, j)]^2}, \quad (28)$$

$$PSNR = 10 \cdot \log_{10} \left( \frac{MAX_R^2}{MSE} \right). \quad (29)$$

where,  $m$  is the total number of pixels in the real image  $R$ ,  $n$  is the total number of pixels in the denoised image  $P$ , and  $MAX_R$  is the maximum possible pixel value of the real image.

By comparing and analyzing the data in Table 1-4, the hybrid denoising method proposed in this paper has the smallest MAE, MSE and NMSE and the largest SNR and PSNR on both Test figure A-E, which indicates that the noise filtering effect is the best, the image quality is the best, the distortion is the lowest, and the impact on the detailed features of the edges of the information in the image is the smallest.

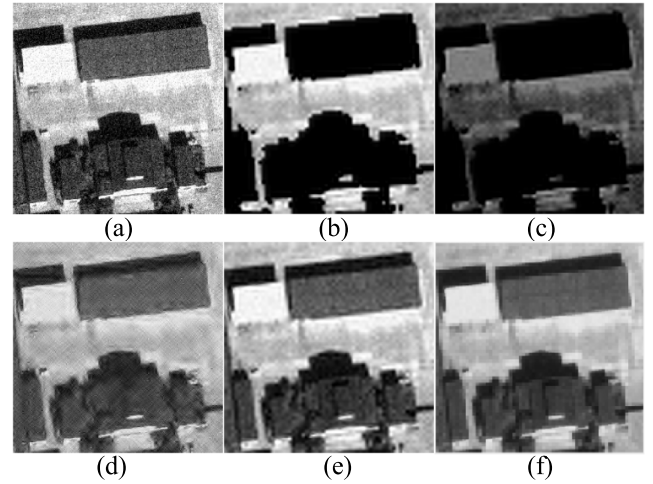


**FIGURE 6.** The results of different denoising algorithms on the Test figure B. (a) Image with Gaussian noise. (b) Hard threshold denoising result graph. (c) Soft threshold denoising result map. (d) Folding threshold denoising result graph. (e) Global threshold denoising result map. (f) Novel TV and WATD hybrid denoising result plot.

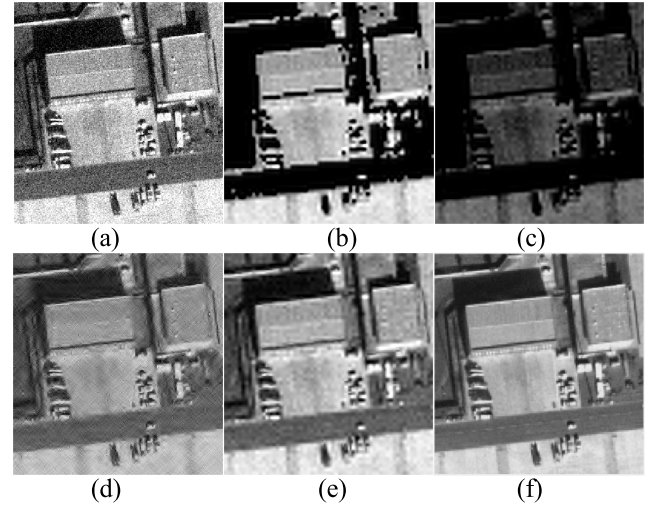


**FIGURE 7.** The results of different denoising algorithms on the Test figure C. (a) Image with Gaussian noise. (b) Hard threshold denoising result graph. (c) Soft threshold denoising result map. (d) Folding threshold denoising result graph. (e) Global threshold denoising result map. (f) Novel TV and WATD hybrid denoising result plot.

### B. RESULTS AND ANALYSIS OF DIFFERENT EDGE DETECTION METHODS

We compare the edge detection algorithm proposed in this paper with the common edge detection algorithms to constitute a comparison experiment in order to verify that the edge detection algorithm proposed in this paper has the best detection effect. We choose the traditional edge detection algorithms Canny [18] and Sobel [17], an ICA algorithm [12] using median filter for noise filtering is proposed on the basis of Canny algorithm, an algorithm for Hed [26] based on deep learning, an algorithm combining Hed and Sobel detectors (ISA1) [27], an improved Sobel algorithm with a 4-direction  $3 \times 3$  convolution kernel (ISA2) [11] and an 8-direction  $5 \times 5$  size of the improved Sobel algorithm (ISA3) [21]



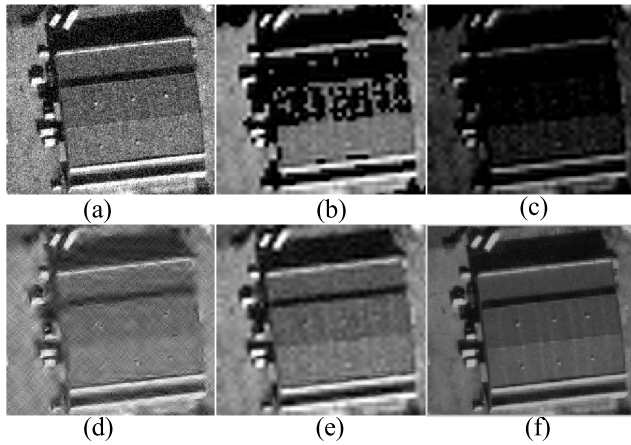


**FIGURE 8.** The results of different denoising algorithms on the Test figure D. (a) Image with Gaussian noise. (b) Hard threshold denoising result graph. (c) Soft threshold denoising result map. (d) Folding threshold denoising result graph. (e) Global threshold denoising result map. (f) Novel TV and WATD hybrid denoising result plot.

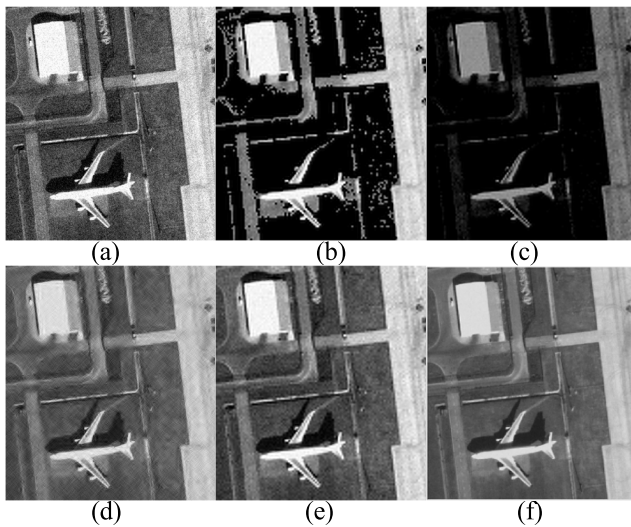


**FIGURE 9.** The results of different denoising algorithms on the Test figure E. (a) Image with Gaussian noise. (b) Hard threshold denoising result graph. (c) Soft threshold denoising result map. (d) Folding threshold denoising result graph. (e) Global threshold denoising result map. (f) Novel TV and WATD hybrid denoising result plot.

are respectively proposed on the basis of Sobel algorithm for comparative experiments. We quantitatively analyze the visual effect of the resultant maps of different edge detection methods in comparative experiments as well as the data on the selection of Eqs. (25)-(29), a quantitative metric of the performance merits of an improved edge detection operator, and the ROC curves [44].

Based on the objective quantized edge detection operator metric proposed by Pratt [44], a new improved edge detection operator quantization metric is proposed, as shown in the following equation:

$$FOM = \frac{1}{\max\{P_R, P_A\}} \sum_{P=1}^{P_A} \frac{1}{1 + \partial d^2}, \partial = \frac{1}{9}. \quad (30)$$

**TABLE 1.** Test figure A objective data results of different denoising methods.

Method	MAE	MSE	NMSE	SNR	PSNR
Hard threshold [33]	11.75	76.16	0.39	4.12	29.31
Soft threshold [32]	48.47	190.26	0.97	0.15	25.34
Folding threshold [39]	3.59	24.93	0.13	8.97	34.16
Global threshold [38]	4.42	34.67	0.18	7.54	32.73
TV and WATD hybrid denoising	3.30	21.04	0.11	9.71	34.90

where,  $P_R$  is the total number of edge pixel points in the real edge image.  $P_A$  is the total number of edge pixel points in the actual detected edge image.  $\partial$  is the scale factor.  $d$  is the Euclidean distance from the line connecting the actual detected edge points to the real edge points. The larger the value of FOM, the better the detection performance.

We introduce the quantitative evaluation criterion of accuracy error for evaluating the performance of edge detection algorithms. In order to verify the authenticity of the detected pixels, ground truth edge images need to be utilized. We assume that  $N_{TP}$  and  $N_{FP}$  are the total number of detected true edge and false edge pixel points, respectively.  $N_{edge}$  is the total number of edge pixels, and  $N_{Non-edge}$  is the total number of non-edge pixels. the larger the area AUC under the ROC curve is, the higher the edge detection accuracy is, and the closer the detection result is to the true value on the ground. FPR and TPR are used as the horizontal and vertical axes of the ROC curve, respectively.

$$TPR = 1 - \frac{N_{TP}}{N_{edge}}, \quad (31)$$

$$FPR = \frac{N_{TP}}{N_{Non-edge}}. \quad (32)$$

The visual effect and quantitative metrics data of the Test figure A for different edge detection algorithms are shown in Fig. 10 and Table 6, respectively. Through analyzing the results of different edge detection algorithms in the visual effect of the preprocessed Test figure A, we can find that the ISA1 and ISA2 can detect most of the edge information of the image, but the output edges are wide, and it is difficult to detect the edge information of the small region. ISA3 has too wide output edges, with a large number of discrete points, not enough smooth edges, and poor detection effect. The boundary of Canny and ICA detection results is blurred from the background data, and the data on the contour line is messy, there is still room for improvement. Sobel has a large number of incomplete edge information detection problems, and the

**TABLE 2. Test figure B objective data results of different denoising methods.**

Method	MAE	MSE	NMSE	SNR	PSNR
Hard threshold [33]	30.55	145.87	0.58	2.36	26.49
Soft threshold [32]	87.43	245.20	0.98	0.10	24.24
Folding threshold [39]	11.16	91.82	0.37	4.37	28.50
Global threshold [38]	9.68	79.93	0.32	4.97	29.10
TV and WATD hybrid denoising	6.10	51.89	0.21	6.84	30.98

**TABLE 3. Test figure C objective data results of different denoising methods.**

Method	MAE	MSE	NMSE	SNR	PSNR
Hard threshold [33]	33.05	133.21	0.54	2.65	26.89
Soft threshold [32]	93.89	238.98	0.97	0.11	24.35
Folding threshold [39]	17.55	127.56	0.52	2.84	27.07
Global threshold [38]	8.89	74.30	0.30	0.64	30.88
TV and WATD hybrid denoising	6.60	52.13	0.22	5.18	29.42

detection effect is not good. Hed can only detect the edges of large buildings, can not recognize the details of small areas of edge features, and the edge detection effect is not good. The MISA algorithm proposed in this paper has a good visual effect and no noise. The contour is clear, the edge is fine, and the anti-creation performance is good.

Analyzing the detection results quantitatively, we can find that the edge detection algorithms proposed in this paper have the lowest values of MAE, MSE, NMSE, and the highest values of SNR, PSNR, which indicates that the resultant map of MISA algorithm is the closest to the real edge map. The value of FOM is the highest compared to the other algorithms, which indicates that the detection performance of MISA algorithm is the best, and the value of AUC is the largest, which indicates that the edge detection results are the most accurate. The FOM values of ISA1, ISA2, and ISA3 algorithms are lower, although they can detect the edge information of large buildings, but the edge line is too wide, and it is difficult to detect the detail area. The values of various evaluation indexes of Canny and Hed algorithms correspond to the analyzed results of the visual effect, but

**TABLE 4. Test figure D objective data results of different denoising methods.**

Method	MAE	MSE	NMSE	SNR	PSNR
Hard threshold [33]	26.05	131.23	0.53	2.80	26.95
Soft threshold [32]	76.05	238.61	0.96	0.20	24.35
Folding threshold [39]	27.20	184.15	0.73	1.32	25.48
Global threshold [38]	6.38	50.99	0.20	6.90	31.06
TV and WATD hybrid denoising	5.60	42.41	0.17	7.70	31.86

**TABLE 5. Test figure E objective data results of different denoising methods.**

Method	MAE	MSE	NMSE	SNR	PSNR
Hard threshold [33]	40.34	165.89	0.66	1.79	25.93
Soft threshold [32]	81.20	246.67	0.98	0.07	24.21
Folding threshold [39]	7.78	68.61	0.27	5.62	29.77
Global threshold [38]	7.31	62.30	0.25	0.04	30.19
TV and WATD hybrid denoising	4.68	42.68	0.17	7.69	31.83

there is still room for improvement. The MAE, MSE, and NMSE values of ICA algorithm are the largest, and the SNR, PSNR, and FOM values are the smallest, which indicates that ICA algorithm has the worst detection performance. Sobel algorithm has lower FOM values and higher MAS, MSE, NMSE values, which indicates that only using the gradient information in the horizontal and vertical directions can not accurately detect the feature information of complex remote sensing images.

Through the analysis of the comparative experimental results of the Test figure B in Fig. 11, we found that the Sobel algorithm only can detect the edge features of large buildings, and cannot detect the edge features of the detailed feature information, with low detection accuracy. Although ICA operator can detect a large amount of edge information, but there are still a large number of leakage detection, the detection effect is not good. The boundary between the contour line and the background data of the detection results of the Canny algorithm is blurred, the details can not be detected, and the accuracy of the detection results is not high. Hed detector can detect most of the edge information, but it is

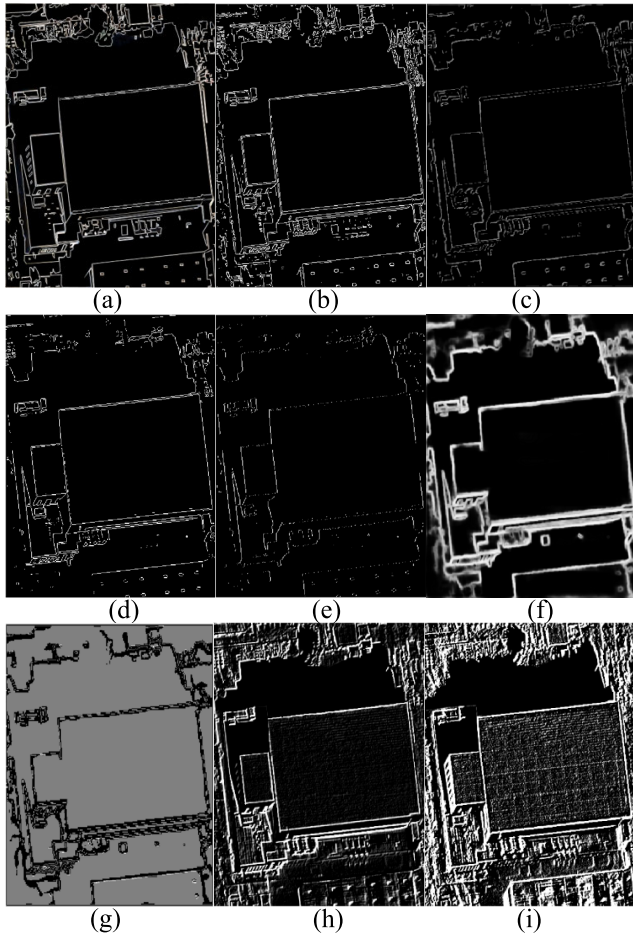


**FIGURE 10.** The results of different edge detection algorithms on Test figure A. (A) Real edge map. (B) MISA algorithm. (C) Canny operator. (D) Sobel operator. (E) ICA algorithm. (F) Hed operator. (G) ISA1 operator. (H) ISA2 algorithm. (I) ISA3 algorithm.

weak for edge feature extraction of detail information. ISA1 can only detect the main edge features, which is not effective. The output edges of ISA2 and ISA3 are too thick, and there are a lot of noise points. The noise immunity is not high, the detection effect is not good, and the detail information processing is difficult. The MISA algorithm proposed in this paper can detect a large amount of detailed information, which is not disturbed by noise, and the visual detection effect is the best.

Through the analysis of the comparative experimental results using different evaluation indexes for the Test figure B in the Table 7, we can find that the performance of the MISA edge detection operator proposed in this paper is still the best, the MAE, MSE, NMSE values of MISA are the lowest, which indicates that the detected edge error is the smallest. The SNR, PSNR values are the largest, which indicates that the MISA operator has the lowest misdetections rate and the best detection performance. The FOM values and AUC values of MISA are the largest, indicating that the detected edge image is the most similar to the real edge map on the ground and has the best effect. By analyzing the seven evaluation

**TABLE 6.** The evaluation metrics of different edge detection algorithms on the test figure A.

Method	MAE	MSE	NMSE	SNR	PSNR	FOM	AUC
MISA	10.89	17.85	0.48	3.17	35.62	0.59	0.69
Canny [18]	19.41	32.05	0.87	0.62	33.07	0.51	0.61
Sobel [18]	18.17	28.80	0.77	1.11	33.54	0.37	0.65
ICA [18]	20.44	32.04	0.87	0.63	33.07	0.22	0.58
Hed [18]	12.94	23.68	0.99	0.05	34.39	0.40	0.67
ISA1 [18]	13.50	25.87	0.69	1.58	34.00	0.19	0.12
ISA2 [18]	15.26	25.56	0.66	1.78	34.23	0.35	0.65
ISA3 [18]	13.82	22.75	0.61	2.11	34.56	0.35	0.61

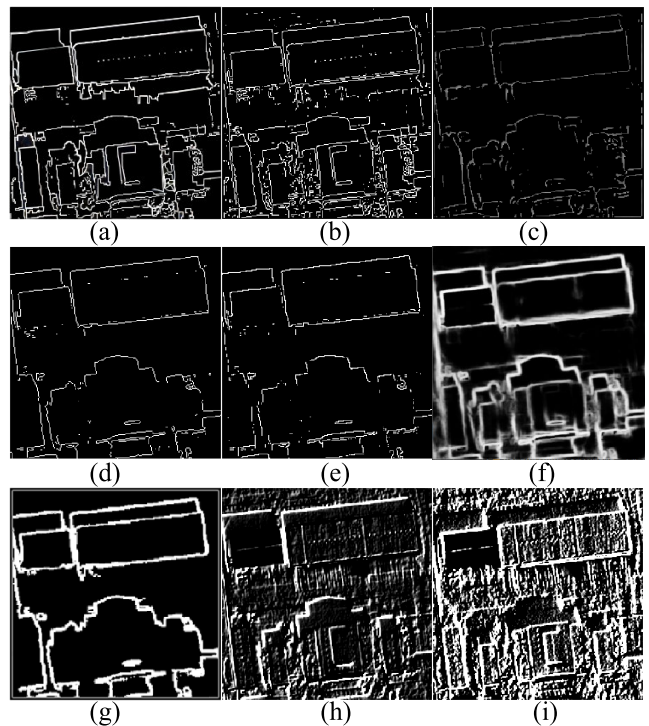


**FIGURE 11.** The results of different edge detection algorithms on Test figure B. (A) Real edge map. (B) MISA algorithm. (C) Canny operator. (D) Sobel operator. (E) ICA algorithm. (F) Hed operator. (G) ISA1 operator. (H) ISA2 algorithm. (I) ISA3 algorithm.

metrics of Hed, ISA1, ISA2, and ISA3 algorithms, we find that their edge detection results are worse than the MISA algorithm, and there are some room for improvement. The MAE, MSE and NMSE values of Canny and ICA algorithms are too large, and the edge detection errors are very large, which make the detection performance bad. The SNR, PSNR values of Sobel algorithm is too low, and the detection performance is bad.

Visually, we can find that in the Fig. 12 the MISA algorithm is the closest to the real edge map of the ground, the edge contour line is more fine, can detect a large number of detail



**TABLE 7.** The evaluation metrics of different edge detection algorithms on the test figure B.

Method	MAE	MSE	NMSE	SNR	PSNR	FOM	AUC
MISA	16.31	26.53	0.49	3.09	33.89	0.51	0.73
Canny [18]	28.02	46.84	0.87	0.62	31.42	0.27	0.62
Sobel [18]	26.15	43.04	0.78	1.05	31.79	0.28	0.63
ICA [18]	29.14	46.55	0.86	0.65	31.45	0.18	0.58
Hed [18]	17.56	32.95	0.97	0.13	32.95	0.47	0.66
ISA1 [18]	21.00	24.99	0.76	1.34	34.15	0.47	0.60
ISA2 [18]	18.05	31.58	0.58	2.34	33.14	0.48	0.65
ISA3 [18]	19.06	32.96	0.61	2.15	32.95	0.49	0.51

**TABLE 8.** The evaluation metrics of different edge detection algorithms on the test figure C.

Method	MAE	MSE	NMSE	SNR	PSNR	FOM	AUC
MISA	20.45	21.44	0.51	2.89	34.82	0.81	0.65
Canny [18]	30.53	30.54	0.73	1.35	33.28	0.53	0.57
Sobel [18]	34.08	47.78	0.84	0.76	31.34	0.52	0.58
ICA [18]	38.95	38.96	0.93	0.29	32.23	0.29	0.52
Hed [18]	17.07	41.04	0.59	2.26	31.99	0.44	0.60
ISA1 [18]	28.66	35.73	0.52	2.86	32.60	0.69	0.51
ISA2 [18]	25.43	28.98	0.70	1.58	33.51	0.66	0.59
ISA3 [18]	23.77	23.78	0.57	2.44	34.37	0.71	0.50

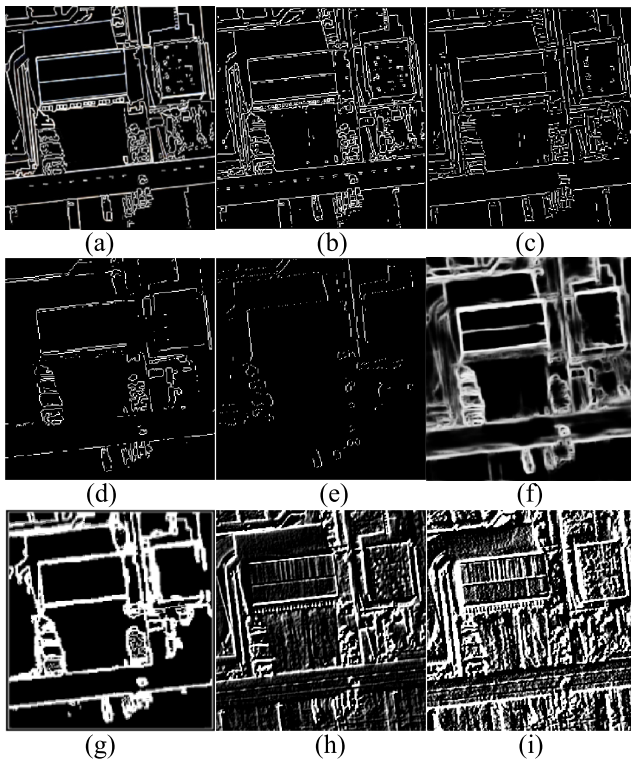


**FIGURE 12.** The results of different edge detection algorithms on Test figure C. (A) Real edge map. (B) MISA algorithm. (C) Canny operator. (D) Sobel operator. (E) ICA algorithm. (F) Hed operator. (G) ISA1 operator. (H) ISA2 algorithm. (I) ISA3 algorithm.

areas, the detection effect is the best, and the edge detection accuracy is the highest. The Canny operator can detect a large number of edge features, but for the detail areas of the feature extraction ability is poor. The Sobel, ICA, and ISA3 algorithm detection results have a large error, the leakage rate is too high. The Hed, ISA1 and ISA2 operators can detect more edge features, but the output contour line is thicker, the detail area features are fuzzy, and the detection effect is not good.

Analyzing the edge detection results of different algorithms in the Test figure C by using Table 8, the MISA algorithm has the smallest values of MAE, MSE, NMSE, and the largest values of SNR, PSNR, FOM and AUC. The MAE, MSE, NMSE values of Canny and ICA algorithms are the largest, indicating that the detection errors are larger. The AUC values of ISA1, ISA2, and ISA3 algorithms are lower, indicating that the detection results are different from the real edge. The Sobel and Hed algorithms have too small SNR, PSNR values, which indicates that the false detection rates are too high and the detection performance are not good.

By analyzing the visual effect of the Test figure image D in Fig. 13, we can find that the edge image detected by the MISA algorithm is the closest to the real edge image, with clear contour lines, and performs the best in terms of visual effect. The Canny, Sobel, and ICA algorithms have a large number of omissions in their visual effect, and there are faults in the contour lines of the edges, so the detection effect are not good. The Hed, ISA1, ISA2 and ISA3 can detect part of the information, and the contour line are coarse and the effect are not good.

The data analysis of different algorithm result maps in the comparison experiments through Table 9. The MISA algorithm proposed in this paper has the smallest values of MAE, MSE, NMSE, and the largest values of SNR, PSNR, FOM and AUC, which indicates that the detection result of MISA algorithm is the closest to the real value of the ground, and the detection edge error is the smallest, which is the same with the result on the visual effect. The MAE, MSE, NMSE values of Canny, Sobel, and ICA are larger, which indicates that the edge detection errors are larger. The MAE, MSE and NMSE values of Hed, ISA1, ISA2 and ISA3 algorithms are slightly higher than those of MISA algorithm. And the SNR, PSNR, FOM, and AUC values are lower than those of MISA algorithm, so there are still room for improvement.

Visually, the MISA algorithm proposed in this paper is the closest to the real edge map on the ground, the edge



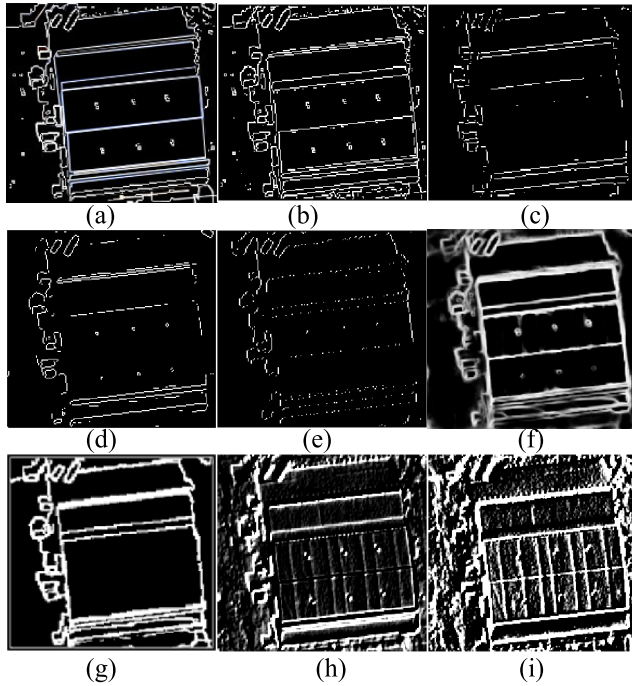


**FIGURE 13.** The results of different edge detection algorithms on Test figure D. (A) Real edge map. (B) MISA algorithm. (C) Canny operator. (D) Sobel operator. (E) ICA algorithm. (F) Hed operator. (G) ISA1 operator. (H) ISA2 algorithm. (I) ISA3 algorithm.

**TABLE 9.** The evaluation metrics of different edge detection algorithms on the test figure D.

Method	MAE	MSE	NMSE	SNR	PSNR	FOM	AUC
MISA	18.02	29.68	0.53	2.77	33.41	0.89	0.73
Canny [18]	29.47	47.52	0.85	0.72	31.36	0.72	0.58
Sobel [18]	28.94	46.53	0.83	0.81	31.45	0.70	0.61
ICA [18]	32.54	51.46	0.92	0.38	31.02	0.71	0.53
Hed [18]	20.06	32.89	0.93	0.30	32.96	0.63	0.67
ISA1 [18]	21.29	26.83	0.76	1.18	33.85	0.75	0.62
ISA2 [18]	20.40	33.58	0.60	2.23	32.87	0.82	0.60
ISA3 [18]	20.38	35.39	0.63	2.00	32.64	0.51	0.53

contour lines are clearly visible, and the edge features are also accurately extracted for the detailed areas around the airplane. By observing Fig. 14, we can obviously find that the edge detection results of Canny and ICA algorithms have discontinuous contour lines. Sobel algorithm can detect the main information edge, but the extraction of edge information for the detail region is weak, there is some room for improvement. Hed algorithm can detect the majority of the edge information, but there are a large number of missed detections, which affects the detection accuracy. The ISA1 can detect some of the edge features, but the edge contour lines are thicker, which is not good. The ISA1 and ISA2

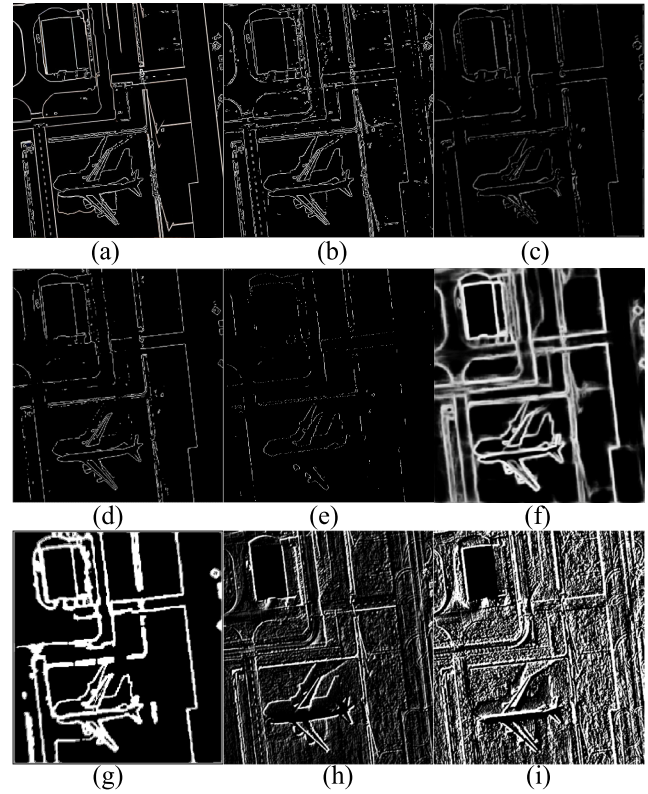


**FIGURE 14.** The results of different edge detection algorithms on Test figure E. (A) Real edge map. (B) MISA algorithm. (C) Canny operator. (D) Sobel operator. (E) ICA algorithm. (F) Hed operator. (G) ISA1 operator. (H) ISA2 algorithm. (I) ISA3 algorithm.

**TABLE 10.** The evaluation metrics of different edge detection algorithms on the test figure E.

Method	MAE	MSE	NMSE	SNR	PSNR	FOM	AUC
MISA	8.50	15.33	0.48	3.07	36.28	0.81	0.77
Canny [18]	17.41	29.06	0.93	0.32	33.50	0.08	0.58
Sobel [18]	15.34	25.27	0.80	0.94	34.10	0.71	0.64
ICA [18]	18.36	29.18	0.93	0.31	33.48	0.47	0.54
Hed [18]	11.02	19.07	0.97	0.15	35.33	0.53	0.71
ISA1 [18]	11.62	19.08	0.56	2.51	37.69	0.62	0.66
ISA2 [18]	11.55	19.30	0.62	2.10	35.27	0.79	0.63
ISA3 [18]	9.95	16.18	0.52	2.87	36.04	0.26	0.49

algorithm has very poor visual effect, and the edge detection accuracy is not high.

By analyzing the data in Table 10, the MAE, MSE, NMSE values of MISA are the smallest, indicating that the MISA algorithm has the smallest error in detecting the edges. The values of SNR, PSNR, FOM and ROC are the largest in the comparative experiments, which indicates that the MISA algorithm has the smallest false positive detection rate, is the

most similar to the real edge maps on the ground, and has the best detection performance. The Canny, Sobel, ICA, Hed, ISA1 and ISA2 algorithms have larger MAE, MSE, NMSE, which indicates that there is a large number of errors and the results are not good. The FOM and AUC values of ISA3 algorithm are small, which indicates that the difference with the real edge map is large and the detection performance is ordinary.

In the comparison experiments, both in the visual effects and qualitative analysis, the edge detection result maps of the MISA algorithm proposed in this paper are the closest to the real edge maps on the ground, with the highest edge detection completeness, and clear and continuous contour lines.

## V. CONCLUSION

According to the characteristics of HRS images which are rich in a large amount of noise and feature information, we propose a hybrid denoising method with total variation and wavelet adaptive threshold, and a novel Sobel edge detection algorithm based on multi-directions to detect feature edges on remote sensing images, so as to propose useful feature information. No matter on the visual effect or data analysis, the hybrid denoising filter proposed in this paper has the best effect to filter out the noise while retaining the image edge feature information without generating pseudo edges. The multi-directional Sobel algorithm edge detection algorithm proposed in this paper has the highest SNR, PSNR, FOM and AUC values and the smallest MAE, MSE and NMSE values in the comparison experiments, which indicates that the algorithm in this paper is the most effective and has continuous edges, strong noise immunity, and is more effective in recognizing the detailed regions. The method proposed in this paper lacks a high-level numerical model to extract semantic features of images. In the future, we will combine the deep learning neural network to realize the elimination of texture interference.

## ACKNOWLEDGMENT

Lu Shi would like to thank Xinwei Yuan for his help and companionship. Lu Shi and Yuefeng Zhao would like to thank the Gaofen-1 satellite image sample provided by the Gaofen-Shandong Center.

## REFERENCES

- [1] J. A. Robert and J. Walter, *Digital Image Processing and Analysis*, vol. 977, pp. 327–392.
- [2] D. R. Menaka, D. R. Janarthanan, and D. K. Deeba, “FPGA implementation of low power and high speed image edge detection algorithm,” *Microprocessors Microsystems*, vol. 75, Jun. 2020, Art. no. 103053, doi: 10.1016/j.micpro.2020.103053.
- [3] J. Abraham and C. Wloka, “Edge detection for satellite images without deep networks,” in *Proc. Comput. Vis. Pattern Recognit.*, 2021, pp. 1–8.
- [4] M. Rajeswari, K. S. Gurumurthy, L. P. Reddy, S. N. Omkar, and J. Senthilnath, “Automatic road extraction based on level set, normalized cuts and mean shift methods,” *Int. J. Comput. Sci. Issues (IJCSI)*, vol. 8, no. 3, pp. 250–257, 2011.
- [5] J. Xi and J.-Z. Zhang, “Edge detection from remote sensing images based on Canny operator and Hough transform,” in *Advances in Computer Science and Engineering*, 2012, pp. 807–814.
- [6] A. Cerovecki, S. Gharahjeh, E. Harirchian, D. Ilin, K. Okhotnikova, and J. Kersten, “Evaluation of change detection techniques using very high resolution optical satellite imagery,” *Preface*, vol. 2, pp. 20–33, Aug. 2015.
- [7] C.-I. Fan and Y.-Y. Ren, “Study on the edge detection algorithms of road image,” in *Proc. 3rd Int. Symp. Inf. Process.*, Oct. 2010, pp. 217–220.
- [8] A. D. Schlosser, G. Szabó, L. Bertalan, Z. Varga, P. Enyedi, and S. Szabó, “Building extraction using orthophotos and dense point cloud derived from visual band aerial imagery based on machine learning and segmentation,” *Remote Sens.*, vol. 12, no. 15, p. 2397, Jul. 2020, doi: 10.3390/rs12152397.
- [9] K. Reda and M. Kedziński, “Detection, classification and boundary regularization of buildings in satellite imagery using faster edge region convolutional neural networks,” *Remote Sens.*, vol. 12, no. 14, p. 2240, Jul. 2020, doi: 10.3390/rs12142240.
- [10] F. Zhang, B. Du, and L. Zhang, “Saliency-guided unsupervised feature learning for scene classification,” *IEEE Trans. Geosci. Remote Sens.*, vol. 53, no. 4, pp. 2175–2184, Apr. 2015, doi: 10.1109/TGRS.2014.2357078.
- [11] J. Chaochao and F. Zhang, “Edge detection based on improved Sobel operator,” in *Detection Based Improved Sobel Operator*, 2016, pp. 129–132.
- [12] P. Topno and G. Murmu, “An improved edge detection method based on median filter,” in *Proc. Devices Integr. Circuit (DevIC)*, Mar. 2019, pp. 378–381.
- [13] T. L. Sung and H. J. Lee, “Depth edge detection using edge-preserving filter and morphological operations,” *Int. J. Syst. Assurance Eng. Manage.*, vol. 11, no. 4, pp. 812–817, Aug. 2020, doi: 10.1007/s13198-019-00881-y.
- [14] P.-L. Shui and F.-P. Wang, “Anti-impulse-noise edge detection via anisotropic morphological directional derivatives,” *IEEE Trans. Image Process.*, vol. 26, no. 10, pp. 4962–4977, Oct. 2017, doi: 10.1109/TIP.2017.2726190.
- [15] S. M. Ismail, L. A. Said, A. G. Radwan, A. H. Madian, and M. F. Abu-ElYazeed, “A novel image encryption system merging fractional-order edge detection and generalized chaotic maps,” *Signal Process.*, vol. 167, Feb. 2020, Art. no. 107280, doi: 10.1016/j.sigpro.2019.107280.
- [16] N.-D. Hoang and Q.-L. Nguyen, “Metaheuristic optimized edge detection for recognition of concrete wall cracks: A comparative study on the performances of Roberts, Prewitt, Canny, and Sobel algorithms,” *Adv. Civil Eng.*, vol. 2018, pp. 1–16, Nov. 2018, doi: 10.1155/2018/7163580.
- [17] T. Peng-o and P. Chaikan, “High performance and energy efficient Sobel edge detection,” *Microprocessors Microsystems*, vol. 87, Nov. 2021, Art. no. 104368, doi: 10.1016/j.micpro.2021.104368.
- [18] D. Sundani, S. Widiyanto, Y. Karyanti, and D. T. Wardani, “Identification of image edge using quantum Canny edge detection algorithm,” *J. ICT Res. Appl.*, vol. 13, no. 2, pp. 133–144, Sep. 2019, doi: 10.5614/itbj.ict.res.appl.2019.13.2.4.
- [19] H. Xu, X. Xu, and Y. Zuo, “Applying morphology to improve Canny operator’s image segmentation method,” *J. Eng.*, vol. 2019, no. 23, pp. 8816–8819, Dec. 2019, doi: 10.1049/joe.2018.9113.
- [20] M. Tavakoli and A. Rosenfeld, “Building and road extraction from aerial photographs,” *IEEE Trans. Syst., Man, Cybern.*, vol. SMC-12, no. 1, pp. 84–91, Jan. 1982.
- [21] L. Han, Y. Tian, and Q. Qi, “Research on edge detection algorithm based on improved Sobel operator,” in *Proc. MATEC Web Conf.*, vol. 309, 2020, p. 3031, doi: 10.1051/mateconf/202030903031.
- [22] R. Chetia, S. M. B. Boruah, and P. P. Sahu, “Quantum image edge detection using improved Sobel mask based on NEQR,” *Quantum Inf. Process.*, vol. 20, no. 1, p. 21, 2021, doi: 10.1007/s11128-020-02944-7.
- [23] W. Liu and L. Wang, “Quantum image edge detection based on eight-direction Sobel operator for NEQR,” *Quantum Inf. Process.*, vol. 21, no. 5, p. 190, May 2022, doi: 10.1007/s11128-022-03527-4.
- [24] W. Kong, J. Chen, Y. Song, Z. Fang, X. Yang, and H. Zhang, “Sobel edge detection algorithm with adaptive threshold based on improved genetic algorithm for image processing,” *Int. J. Adv. Comput. Sci. Appl.*, vol. 14, no. 2, pp. 1–16, 2023, doi: 10.14569/ijacsa.2023.0140266.
- [25] R. Damasevicius, R. Maskeliunas, M. Wozniak, D. Polap, T. Sidekierskiene, and M. Gabryel, “Detection of saliency map as image feature outliers using random projections based method,” in *Proc. 13th Int. Comput. Eng. Conf. (ICENCO)*, Dec. 2017, pp. 85–90.
- [26] S. Xie and Z. Tu, “Holistically-nested edge detection,” in *Proc. IEEE Int. Conf. Comput. Vis. (ICCV)*, Dec. 2015, pp. 1395–1403.
- [27] F. Li, X. Du, L. Zhang, and A. Liu, “Image feature fusion method based on edge detection,” *Inf. Technol. Control*, vol. 52, no. 1, pp. 5–24, Mar. 2023, doi: 10.5755/j01.itc.52.1.31549.

- [28] S. Karanwal, "Implementation of edge detection at multiple scales," *Int. J. Eng. Manuf.*, vol. 11, no. 1, pp. 1–10, Feb. 2021, doi: [10.5815/ijem.2021.01.01](https://doi.org/10.5815/ijem.2021.01.01).
- [29] R. Tian, G. Sun, X. Liu, and B. Zheng, "Sobel edge detection based on weighted nuclear norm minimization image denoising," *Electronics*, vol. 10, no. 6, p. 655, Mar. 2021, doi: [10.3390/electronics10060655](https://doi.org/10.3390/electronics10060655).
- [30] D. L. Donoho and I. M. Johnstone, "Adapting to unknown smoothness via wavelet shrinkage," *J. Amer. Stat. Assoc.*, vol. 90, no. 432, pp. 1200–1224, Dec. 1995.
- [31] S. Peng, R. Chen, B. Yu, M. Xiang, X. Lin, and E. Liu, "Daily natural gas load forecasting based on the combination of long short term memory, local mean decomposition, and wavelet threshold denoising algorithm," *J. Natural Gas Sci. Eng.*, vol. 95, Nov. 2021, Art. no. 104175, doi: [10.1016/j.jngse.2021.104175](https://doi.org/10.1016/j.jngse.2021.104175).
- [32] W. Chen, J. Li, Q. Wang, and K. Han, "Fault feature extraction and diagnosis of rolling bearings based on wavelet thresholding denoising with CEEMDAN energy entropy and PSO-LSSVM," *Measurement*, vol. 172, Feb. 2021, Art. no. 108901, doi: [10.1016/j.measurement.2020.108901](https://doi.org/10.1016/j.measurement.2020.108901).
- [33] L. Jing-Yi, L. Hong, Y. Dong, and Z. Yan-Sheng, "A new wavelet threshold function and denoising application," *Math. Problems Eng.*, vol. 2016, pp. 1–8, 2016, doi: [10.1155/2016/3195492](https://doi.org/10.1155/2016/3195492).
- [34] F. Yang and T. Le-Ngoc, "GGD model of extrinsic information with dynamic parameter assignment for turbo decoder," *IEEE Trans. Wireless Commun.*, vol. 3, no. 5, pp. 1508–1513, Sep. 2004, doi: [10.1109/twc.2004.834700](https://doi.org/10.1109/twc.2004.834700).
- [35] S. G. Chang, B. Yu, and M. Vetterli, "Adaptive wavelet thresholding for image denoising and compression," *IEEE Trans. Image Process.*, vol. 9, no. 9, pp. 1532–1546, 2000, doi: [10.1109/83.862633](https://doi.org/10.1109/83.862633).
- [36] L. I. Rudin, S. Osher, and E. Fatemi, "Nonlinear total variation based noise removal algorithms," *Phys. D, Nonlinear Phenomena*, vol. 60, nos. 1–4, pp. 259–268, Nov. 1992.
- [37] A. Chambolle, V. Caselles, and D. Cremers, "An introduction to total variation for image analysis," in *Theoretical Foundations and Numerical Methods for Sparse Recovery*, 2010, pp. 263–340.
- [38] Z. Jianhua, Z. Qiang, Z. Jinrong, S. Lin, and W. Jilong, "A novel algorithm for threshold image denoising based on wavelet construction," *Cluster Comput.*, vol. 22, no. S5, pp. 12443–12450, Sep. 2019, doi: [10.1007/s10586-017-1655-0](https://doi.org/10.1007/s10586-017-1655-0).
- [39] G. Wang, "Improved adaptive threshold soft-hard compromise curvelet image denoising technology," *Aeronaut. Comput. Technol.*, vol. 39, no. 1, pp. 92–97, 2009.
- [40] K. Park, M. Chae, and J. H. Cho, "Image pre-processing method of machine learning for edge detection with image signal processor enhancement," *Micromachines*, vol. 12, no. 1, p. 73, Jan. 2021, doi: [10.3390/mi12010073](https://doi.org/10.3390/mi12010073).
- [41] K. Luo, L. Chen, W. Liang, and H. Weng, "A dual-scale morphological filtering method for composite damage identification using FBP," *Mech. Syst. Signal Process.*, vol. 184, Feb. 2023, Art. no. 109683, doi: [10.1016/j.ymsp.2022.109683](https://doi.org/10.1016/j.ymsp.2022.109683).
- [42] X. Y. Zhao, G. Y. Liu, Y. T. Sui, M. Xu, and L. Tong, "Denoising method for Raman spectra with low signal-to-noise ratio based on feature extraction," *Spectrochimica Acta A, Mol. Biomolecular Spectrosc.*, vol. 250, Apr. 2021, Art. no. 119374, doi: [10.1016/j.saa.2020.119374](https://doi.org/10.1016/j.saa.2020.119374).
- [43] D. Poobathy and R. M. Chezian, "Edge detection operators: Peak signal to noise ratio based comparison," *Int. J. Image, Graph. Signal Process.*, vol. 6, no. 10, pp. 55–61, Sep. 2014, doi: [10.5815/ijigsp.2014.10.07](https://doi.org/10.5815/ijigsp.2014.10.07).
- [44] J. Jing, S. Liu, G. Wang, W. Zhang, and C. Sun, "Recent advances on image edge detection: A comprehensive review," *Neurocomputing*, vol. 503, pp. 259–271, Sep. 2022, doi: [10.1016/j.neucom.2022.06.083](https://doi.org/10.1016/j.neucom.2022.06.083).



**LU SHI** (Student Member, IEEE) received the bachelor's degree from Jinan University. She is currently pursuing the master's degree in electronic information with the School of Physics and Electronic Science, Shandong Normal University. Her current research interests include shadow detection and image processing in high resolution images.



**YUEFENG ZHAO** (Member, IEEE) received the Doctor of Science degree from the Hefei Institute of Physical Science of Chinese Academy of Sciences (Anhui Institute of Optics and Machinery), in 2007. Currently, he is the Deputy Director of the Academic Affairs Office, Shandong Normal University. His main research interest includes hyperspectral imaging technology.

...